Chemical Engineering Journal 483 (2024) 149007

Contents lists available at ScienceDirect

Chemical Engineering Journal

journal homepage: www.elsevier.com/locate/cej

In-Situ synthesis of NbC Nanoparticle-Decorated Polyimide-Derived graphene for enhanced thermal management

Yu-Sheng Hsiao [a], Chao-Yuan Lin [b], Lin-Yang Weng [a], Chun-Han Hsu [a], Ta-Hung Cheng [a,c], Jen-Hsien Huang [d], Nian-Jheng Wu [e], Wei Kong Pang [f], Shih-Chieh Hsu [g,*], Huei Chu Weng [h,*], Yu-Ching Huang [c,*]

[a] Department of Materials Science and Engineering, National Taiwan University of Science and Technology, No. 43, Sec. 4, Keelung Road, Da-an District, Taipei 10607, Taiwan
[b] Department of Research and Development, TransformBIZ Ltd., Rm. 906A, 9F., No. 502, Sec. 2, Ren'ai Rd., Linkou Dist., New Taipei City 244, Taiwan
[c] Department of Materials Engineering, Ming Chi University of Technology, 84 Gungjuan Rd., Taishan District, New Taipei City 24301, Taiwan
[d] Department of Green Material Technology, Green Technology Research Institute, CPC Corporation, No.2, Zuonan Rd., Nanzi District, Kaohsiung City 81126, Taiwan
[e] Université Paris-Saclay, CNRS, Institut des Sciences Moléculaires d'Orsay, 91405 Orsay, France
[f] Faculty of Engineering, Institute for Superconducting & Electronic Materials, University of Wollongong, Wollongong NSW, Australia
[g] Department of Chemical and Materials Engineering, Tamkang University, No. 151, Yingzhuan Road, Tamsui District, New Taipei City 25137, Taiwan
[h] Department of Mechanical Engineering, Chung Yuan Christian University, No. 200, Chungpei Rd, Chungli District, Taoyuan City 32023, Taiwan

ARTICLE INFO

Keywords:
Thermal management
polyimide-derived graphene (PDG)
niobium carbide (NbC)
Solar-driven interfacial water evaporation

ABSTRACT

Thermal management and heat dissipation are universal challenges related to high-power systems. Graphene and its related composite materials exhibit the potential for widespread application as thermal management materials owing to their high thermal conductivity and emissivity. In this study, we synthesize polyimide (PI)-derived graphene (PDG) incorporated with NbC nanoparticles via CO_2 laser scribing on Nb precursor-containing PI sheets. The resultant NbC-decorated PDG (NbC-PDG) shows improved thermal conductivity (0.70 W/m·K) compared with bare PDG (0.24 W/m·K). We use NbC-PDG as an efficient heat sink for industrial computers (ICs), light-emitting diode (LED) modules, and lithium-ion batteries (LIBs). The equilibrium temperature of the applications can be reduced significantly by the NbC-PDG layer owing to its excellent radiation heat transfer. After integration of the NbC-PDG heat sink, the equilibrium temperatures of the IC, LED module, and LIB decreased by 8.1, 9.9, and 7.3 °C, respectively. Accordingly, the performance, efficiency, and lifetime of optoelectronic and electrochemical systems can be enhanced considerably. The NbC-PDG composite with broadband absorption and excellent photothermal properties can be applied for efficient solar–thermal energy conversion. Additionally, we fabricate an NbC-PDG-deposited melamine sponge via spray coating and evaluate its performance in solar-driven desalination and water purification.

1. Introduction

Thermal management refers to the process of controlling the temperature of electronic devices to avoid overheating, improve efficiency, and ensure proper functioning and longevity. Effective thermal management is becoming increasingly critical as technology advances and devices become more compact and powerful. Most electronic component failures are caused by overheating due to nonhomogeneous heat accumulation and dissipation [1,2]. Unsatisfactory thermal management can result in the formation of hotspots and temperature gradients across a system. Localized areas with high temperatures typically exhibit reduced performance, accelerated component aging, potential system failure, and safety issues [3]. Furthermore, temperature gradients can induce thermal expansion and generate mechanical stress in electronic devices [4]. Therefore, highly efficient thermal management techniques must be devised to satisfy the demands of modern applications.

Generally, heat is dissipated from electronic components via thermal conduction and convection [5]. This involves the rapid transfer of heat from a heat source to a medium with high thermal conductivity, such as copper- or aluminum-based heat sinks, followed by the dissipation of

* Corresponding authors.
E-mail addresses: 137422@o365.tku.edu.tw (S.-C. Hsu), hcweng@cycu.edu.tw (H. Chu Weng), huangyc@mail.mcut.edu.tw (Y.-C. Huang).

https://doi.org/10.1016/j.cej.2024.149007
Received 26 September 2023; Received in revised form 13 December 2023; Accepted 21 January 2024
Available online 26 January 2024

excess heat into the surrounding environment using fans to enhance airflow through forced convective heat transfer. However, owing to technological progress to satisfy the requirements for integrated components, higher voltages/currents, and miniaturization, a space for fan installation is almost non-existent. In such cases, radiation heat transfer contributes significantly to heat dissipation as it does not require any medium or space. Heat transfer through thermal radiation is solely based on temperature difference. However, most metallic surfaces have a relatively low emissivity in the infrared spectrum and cannot efficiently transfer heat via thermal radiation. Therefore, the surface modification of metallic heat sinks with high emissivity increases the radiative capability required to satisfy the demands of current applications [6–8].

In recent decades, graphene, which is a two-dimensional monolayer of graphite, has received significant attention owing to its high thermal conductivity [9,10], high emissivity [11], and excellent chemical stability. Compared with chemical vapor deposition [12] as well as ion-mediated assembly [13] and self-assembly methods [14], spray coating [15] is a simpler approach that is applicable over large areas to modify metallic heat sinks with high geometric complexity. However, graphene dispersions for spray coating require the use of polymeric binders to enhance the physical adhesion between the graphene layer and substrate. Although a graphene-modified layer can increase emissivity for better thermal radiation capability, the presence of thermally insulating polymers creates additional thermal resistance, which is not conducive to thermal conduction. Therefore, balance must be achieved between the desired emissivity enhancement and the potential disadvantage of increased thermal resistance. In this regard, a modified graphene/polymer resin with high thermal conductivity for spray coating must be developed.

In 2014, Tour et al. first reported a facile and scalable approach to synthesize three-dimensional (3D) porous graphene using polyimide (PI) as the carbon source via a commercial CO_2 infrared laser platform [16]. The resultant PI-derived graphene (PDG), which features a high surface area, electrical conductivity, and tunable morphology, has been used in a wide range of applications, including energy storage [17,18], sensors [19], electrocatalysis [20], and electrothermal heaters [21]. Many fillers such as metal oxides [22], carbon nanotubes [23], conducting polymers [24], and transition metal carbides [25,26] have been used to further enhance the thermal conductivity of graphene. Among these candidates, NbC has attracted considerable interest based on its promising properties, such as high chemical stability, high hardness [27], low thermal expansion coefficient [28], and great thermal conductivity [29]. In general, NbC can be prepared by thermally annealing the niobium oxides and carbonaceous materials in reducing hydrogen atmospheres at high temperatures [30]. However, the carbothermal reduction method is energy- and time-intensive and is difficult to produce nanocrystalline NbC due to the high annealing temperature.

In this study, we propose a one-step route for preparing a PDG composite decorated with NbC nanoparticles via CO_2 laser induction. With the incorporation of NbC nanoparticles into the PDG, the thermal conductivity of the NbC-PDG/polymer resin composite is improved significantly. The radiative heat dissipation performances of the NbC-PDG coatings are evaluated. Both a LED module and LIBs coated the NbC-PDG composite exhibit a significant decrease in the equilibrium temperature, thus resulting in higher efficiency and a prolonged lifespan. In addition, the NbC-PDG coatings exhibit promising solar-thermal conversion and water purification/desalination owing to their broadband absorption. Additionally, an NbC-PDG-modified melamine sponge (MS) for solar-driven interfacial desalination is demonstrated.

2. Experimental section

2.1. Preparation of NbC-PDG composite

In this study, pyromellitic dianhydride and 4,4́-oxydianiline–based poly(amic acid) (PAA) (15.0–16.0 wt% in NMP, Sigma-Aldrich) were used as the precursor solutions for the formation of a PI sheet. Various amounts of $Nb(HC_2O_4)_5{\cdot}xH_2O$ (19.9 % Nb_2O_5 min, Alfa Aesar) (0, 5, 10, 15, and 20 wt%) were dissolved in the PAA solution [12 wt% in N-methyl-2-pyrrolidone (NMP, 99.5 %, Sigma-Aldrich)] under continuous stirring for 2 h. The $Nb(HC_2O_4)_5$/PAA solution was cast on Cu foil using the doctor blade method. Subsequently, the cast films were dried at 160 °C for 1 h to evaporate the NMP solvent and then hard cured at 350 °C under N_2 atmosphere for 2 h to convert PAA into PI. Next, laser scribing process was conducted on the $Nb(HC_2O_4)_5$/PI film using a 10.6 μm CO_2 laser system (Universal Laser Systems, VLS3.50) with a focused beam featuring a diameter of approximately 38 μm (HPDFO™, dual focusing lenses with a collimator). All the samples were prepared under ambient conditions using 20 % speed and 1000 pulses per inch.

2.2. Preparation of NbC-PDG dispersion for spray coating

The NbC-PDG composites obtained from the laser-scribing process were scraped off and then collected. The NbC-PDG was added in 2-butanone (99 %, Sigma-Aldrich) with an epoxy resin (15 wt%) purchased from Transform Biz Enterprise Co., Ltd (CF733-Al-03). The mixture was dispersed by vigorous mechanical agitation for 1 h and then treated with a high-power sonicator for 30 min to form a stable dispersion. The NbC-PDG dispersion was then cast on an Al heat sink or various optoelectronic and electrochemical devices, followed by heating treatment at 80 °C overnight to remove the 2-butanone.

2.3. Characterization

Details of the material characterizations are provided in the Supporting Information.

3. Results and discussion

In this study, we performed CO_2 laser scribing to prepare NbC-decorated PDG; the scheme for synthesizing NbC-PDG is shown in Fig. 1a. First, $Nb(HC_2O_4)_5$ was added to the PAA solution and mixed until it dissolved to form a uniform precursor solution. Subsequently, the dissolved precursor solution was deposited onto a Cu foil for blade coating, followed by thermal imidization [31] at 350 °C under N_2 atmosphere to achieve a PI/$Nb(HC_2O_4)_5$ film. The PI/$Nb(HC_2O_4)_5$ film was irradiated with CO_2 laser in air to form a PDG. During the CO_2 irradiation, $Nb(HC_2O_4)_5$ was converted into NbC because of the elevated temperature and hypoxic conditions. The X-ray diffraction (XRD) patterns of NbC-PDG composites with different weight percentages of Nb$(HC_2O_4)_5$ are presented in Fig. 1b. The pristine PDG shows two diffraction peaks at 25.9° and 43.1°, which are assigned to (0 0 2) and (1 0 0) planes, respectively, and indicate its graphitic crystal structure [32] with an interlayer distance of ~ 3.44 Å from the (0 0 2) plane. For the NbC-PDG samples, four additional peaks at 2θ values of 34.4°, 40.1°, 58.1°, and 69.5° were indicated, which were assigned to the (1 1 1), (2 0 0), (2 2 0), and (3 1 1) planes of the cubic NbC phase, respectively (JCPDF card no. 38–1364) [33]. Furthermore, as the content of Nb$(HC_2O_4)_5$ increased from 0 to 20 wt%, the XRD intensity of NbC increased, thus indicating an improved crystalline structure. The saturation concentration of $Nb(HC_2O_4)_5$ was approximately 20 wt%. When the concentration of $Nb(HC_2O_4)_5$ in PAA exceeded 20 wt%, precipitation occurred and could not be completely dissolved. The Nb concentrations were determined via energy-dispersive X-ray spectroscopy (EDS) point analysis, and the results are shown in Fig. 1c. As expected, when the concentration of $Nb(HC_2O_4)_5$ increased from 0 to 20 wt%, the concentration of Nb increased accordingly. Thermogravimetric analysis (TGA) was performed to quantitatively analyze the NbC content of the PDG. Fig. 1d shows the TGA profiles of the pristine PDG and NbC-PDG (20 wt %). The pristine PDG and NbC-PDG underwent the most significant weight loss at 550 °C and 515 °C at decomposition temperatures of

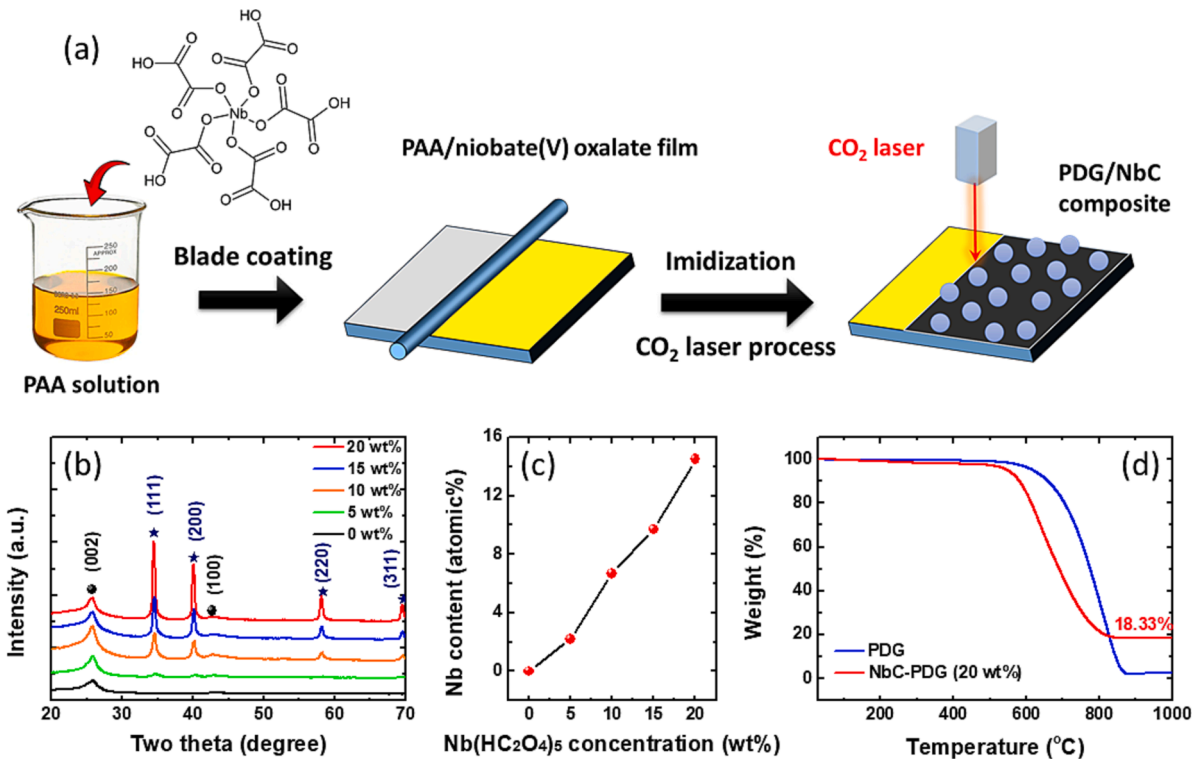

Fig. 1. Preparation of NbC-PDG composite. (a) Schematic illustration of synthesis route of NbC-PDG (b) XRD patterns (c) elemental analysis and (d) TGA profiles of NbC-PDG with various NbC contents.

618 °C and 548 °C (T95), respectively, thus indicating the thermal stability of the NbC-PDG become poorer. We speculate the poor thermal stability of the NbC-PDG was resulted from the unreacted precursors remaining within NbC-PDG (see the Fig. 3e).

After heating at 1000 °C, the pristine PDG showed almost no residual. By contrast, the final weight of the NbC-PDG was 18.33 % at 1000 °C, which is attributed to the NbC nanoparticles.

Transmission electron microscopy (TEM) was performed to monitor the nanostructure of the NbC-PDG composites with various $Nb(HC_2O_4)_5$ concentrations. As shown in Fig. 2a, the pristine PDG exhibited a few-layer graphitic sheet with a smooth surface. Upon careful observation, it can be noticed that within these sheet-like graphene structures, there also exist some fiber-like structure as indicated by the arrow. Fig. 2b shows that miniscule NbC nanoparticles were sparsely distributed on the NbC-PDG (5 wt%) surface. The number and grain size of the NbC nanoparticles decorated on the PDG surface increased gradually with the $Nb(HC_2O_4)_5$ concentration, as depicted in Fig. 2c–d. A magnified image of the decorated NbC nanoparticle is presented in Fig. 2f, which shows an approximately spherical morphology with particle sizes ranging from 10 to 50 nm (Fig. 2e). Furthermore, the lattice fringes with an interplanar distance of 0.35 nm (Fig. S1) can be observed at the upper right section of Fig. 2f, which is consistent with the (0 0 2) plane of graphene. The morphology of the NbC-PDG composite (20 wt%) was further characterized using high-angular annular dark-field scanning TEM (HAADF-STEM), as shown in Fig. 2g and 2 h, which clearly show the deposition of NbC nanoparticles on the PDG surface. EDS mapping was performed to confirm the chemical composition. As shown in Fig. 2i–j, the EDS mappings indicate the presence of Nb and C in the NbC domain. However, extremely weak oxygen signals were observed, as shown in Fig. 2k, which suggests the partial oxidation of the NbC nanoparticles.

The chemical states of the NbC-PDG (20 wt%) composites were examined via X-ray photoelectron spectroscopy (XPS) analysis. The XPS survey spectra presented in Fig. 3a confirmed the presence of C, Nb, and O in the NbC-PDG composite without any contamination. Fig. 3b–d show a comparison of the high-resolution C 1 s spectra of PI, the PDG, and the NbC-PDG. The C 1 s spectrum of PI can be deconvoluted into six functional groups: C—C (285.4 eV), C=C (284.1 eV), C–H (283.4 eV), C—N (284.9 eV), C—O (286.6 eV), and C=O (287.9 eV) bonds [34]. After laser treatment, the C—N and C—H groups in the PI vanished, and the C=O and C—O groups in the C1s XPS spectra of both the PDG and NbC-PDG weakened significantly. This indicates the successful removal of most of the functional groups and the conversion of PI into graphene. Compared with the C 1 s spectrum of the PDG, that of the NbC-PDG shows an additional peak at 282.8 eV, which can be associated with the Nb-C bond in the NbC phase [35,36]. Moreover, the NbC-PDG showed pronounced Nb 3d XPS signals (Fig. 3e), whereas no Nb 3d signal was detected in the PDG sample (Fig. 3f). The convoluted spectrum of Nb 3d in the NbC-PDG comprised multiple oxidation states, including NbC and three different niobium oxides (NbC_xO_y, NbO_2, and Nb_2O_5) [37]. This result is consistent with the EDS results (Fig. 2k). The NbC_xO_y signal observed in NbC-PDG sample indicated that some Nb (HC_2O_4) precursor cannot be completely converted into NbC. The unreacted precursors remaining within NbC-PDG may result in poor thermal stability as shown in Fig. 1d.

Fig. 4a shows the Raman spectra of the pristine and modified PDG with various NbC contents. All samples showed three prominent peaks associated with the D (1343 cm^{-1}), G (1579 cm^{-1}), and 2D bands (2694 cm^{-1}). The I_{2D}/I_G ratios of the five samples were approximately 0.45, thus implying that they were multilayer graphene structures and that the number of layers could not be altered upon decoration with NbC nanoparticles. However, the I_D/I_G ratio of PDG decreased gradually from 0.98 to 0.80 as the NbC content increased, thus suggesting that decorating with NbC can improve the graphitization degree. Scanning electron microscopy (SEM) images of the pristine PDG and NbC-PDG are shown in Fig. 4b and 4c, respectively. Most PDG exhibited a porous fiber structure; however, a few sheet-like structures can still be observed as indicated in Fig. 4b, which is consistent with the findings of previous studies [19,38,39]. By contrast, the NbC-PDG (20 wt%) exhibited a sheet-like morphology with a lateral size ranging between 0.25 and 1.5

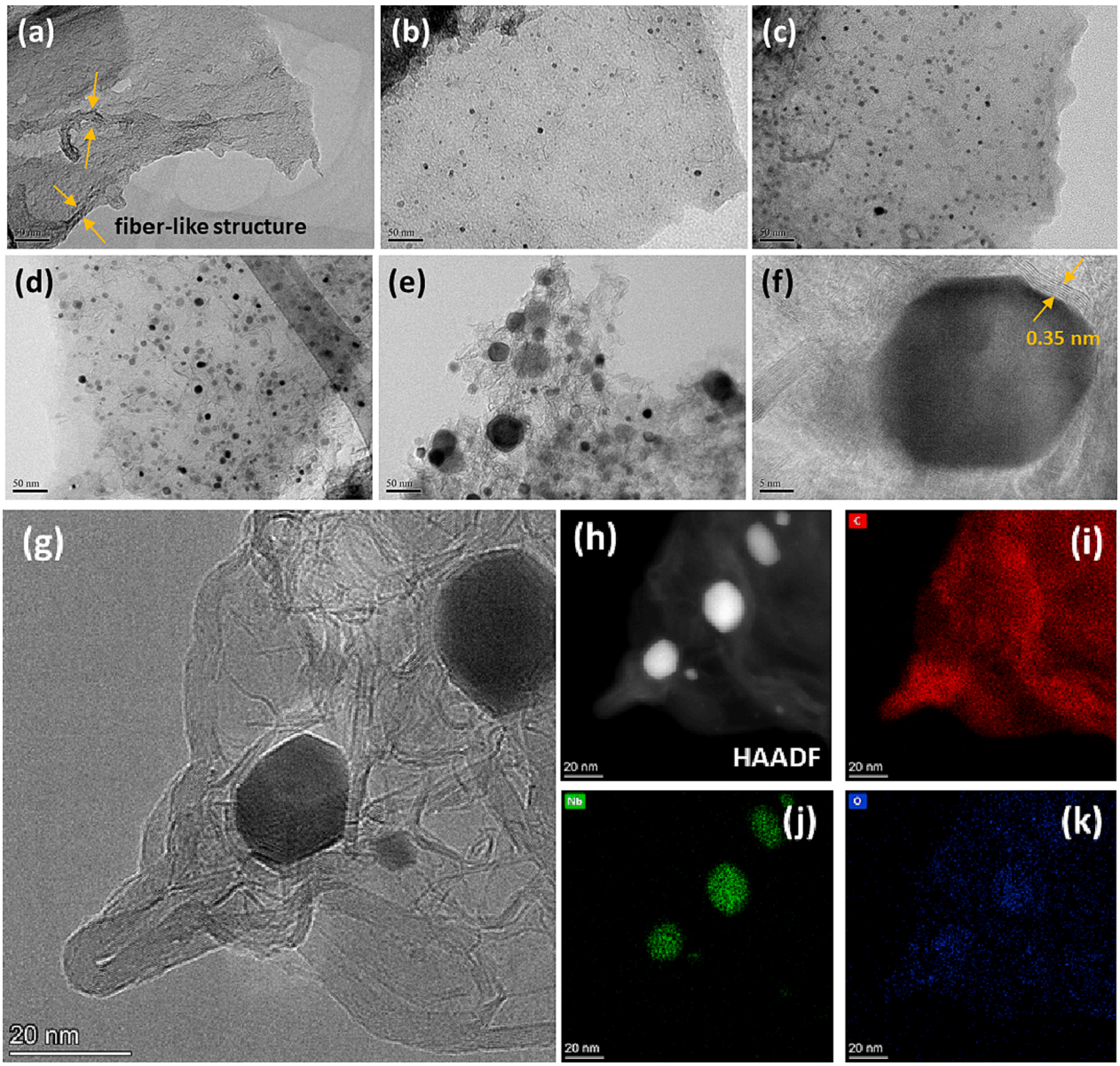

Fig. 2. Morphological investigation of NbC-PDG. TEM image of NbC-PDG with different $Nb(HC_2O_4)_5$ concentrations (a) 0 wt% (b) 5 wt% (c) 10 wt% (d) 15 wt% (e, f) 20 wt%. (g, h) HAADF-STEM of NbC-PDG (20 wt%) and corresponding EDS mapping of (i) C, (j) Nb, and (k) O.

μm. The nitrogen adsorption–desorption isotherms of the PDG and NbC-PDG are shown in Fig. S2. The surface areas of the PDG and NbC-PDG were calculated to be 285.3 and 175.1 m^2/g, respectively. The smaller surface area of the sheet-like NbC-PDG composite suggests its solid structure, which is favorable for the electric and thermal conductivities. The sheet resistances of the as-prepared PDG are shown in Fig. 4d. As the NbC content increased, sheet resistance of the NbC-PDG decreased gradually, which indicates improved electrical conductivity. To further investigate the effect of the decorated NbC nanoparticles on the PDG, the thermal conductivities of the composites incorporating NbC-PDG and the epoxy resin were characterized using the hot-disk method. The corresponding results as a function of PDG and NbC-PDG loadings are shown in Fig. 4e. The neat epoxy resin exhibited a low thermal conductivity of 0.24 W/m·K. The thermal conductivities of the epoxy composites containing PDG and NbC-PDG fillers increased with the filler loading. Thermal conductivity of both the PDG/epoxy and NbC-PDG/epoxy composites improved significantly. At a filler loading of 5 wt%, the thermal conductivity of the NbC-PDG-based composite increased to 0.70 W/m·K, which corresponded to an increase by 191.6 % compared with that of neat epoxy resin. In fact, this value is 1.27 times greater than that of the PDG-based composite (0.55 W/m·K). The improved electrical and thermal conductivities observed after modification with NbC nanoparticles can be ascribed to the increased degree of graphitization, desirable lateral structure, and high conductivity of NbC nanoparticles [33,40]. Radiative heat transfer was significantly affected by the surface emissivity of the substrate. The average values for both the Al and NbC-PDG/Al substrates were measured using a previously reported method [41], as shown in Fig. 4f. The emissivity of the NbC-PDG/Al substrate was notably higher (0.93) than that of the bare Al substrate (0.16). These results indicate that the heat dissipation capability of the Al heat sink modified with the NbC-PDG composite can be further enhanced through radiative heat transfer.

To further evaluate the thermal dissipation capability of the NbC-PDG composite, we modified a commercial Al heat sink with the NbC-PDG via spray coating (Fig. 5a). Photographs of the bare and modified heat sinks are shown in Fig. 5a. The experimental setup illustrated in Fig. 5b was employed to evaluate the heat dissipation performance of the as-prepared NbC-PDG-modified heat sink. An electric heater was

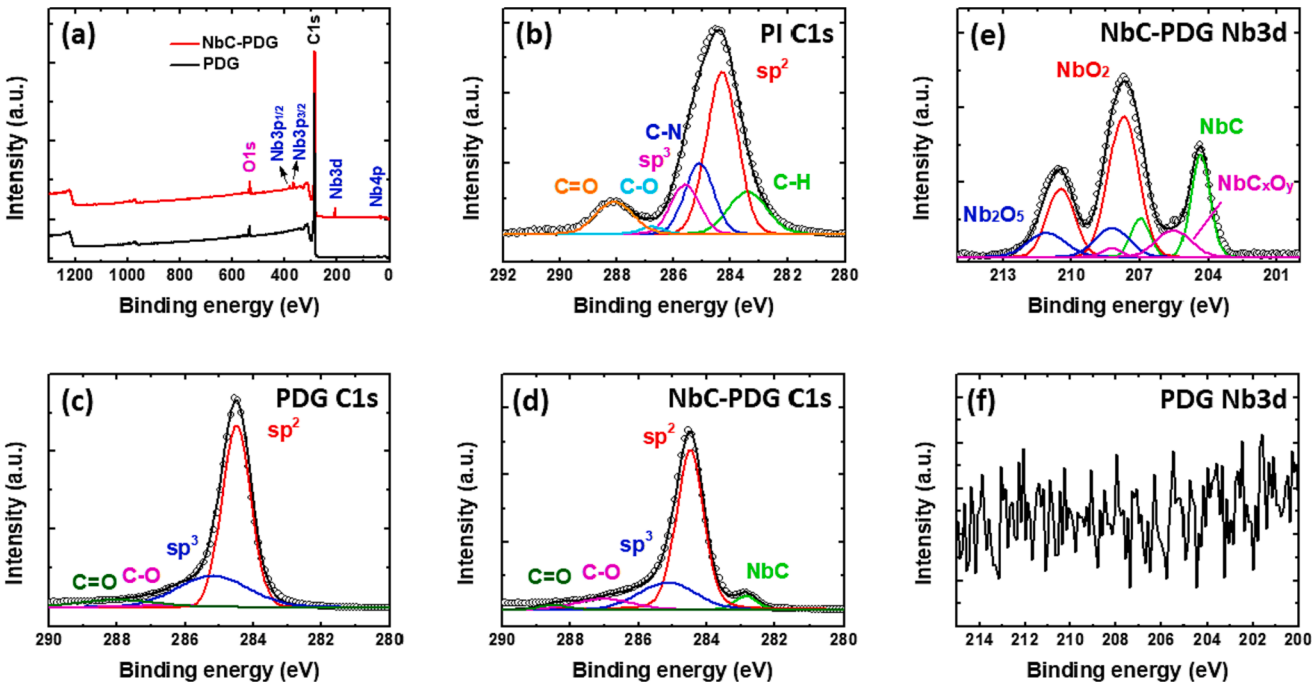

Fig. 3. Chemical composition analysis of NbC-PDG. (a) XPS survey of PDG and NbC-PDG peak deconvolution of C 1 s XPS spectrum of (b) PI (c) PDG and (d) NbC-PDG and peak deconvolution of C 1 s XPS and Nb 3d XPS spectra of (e) NbC-PDG and (f) PDG.

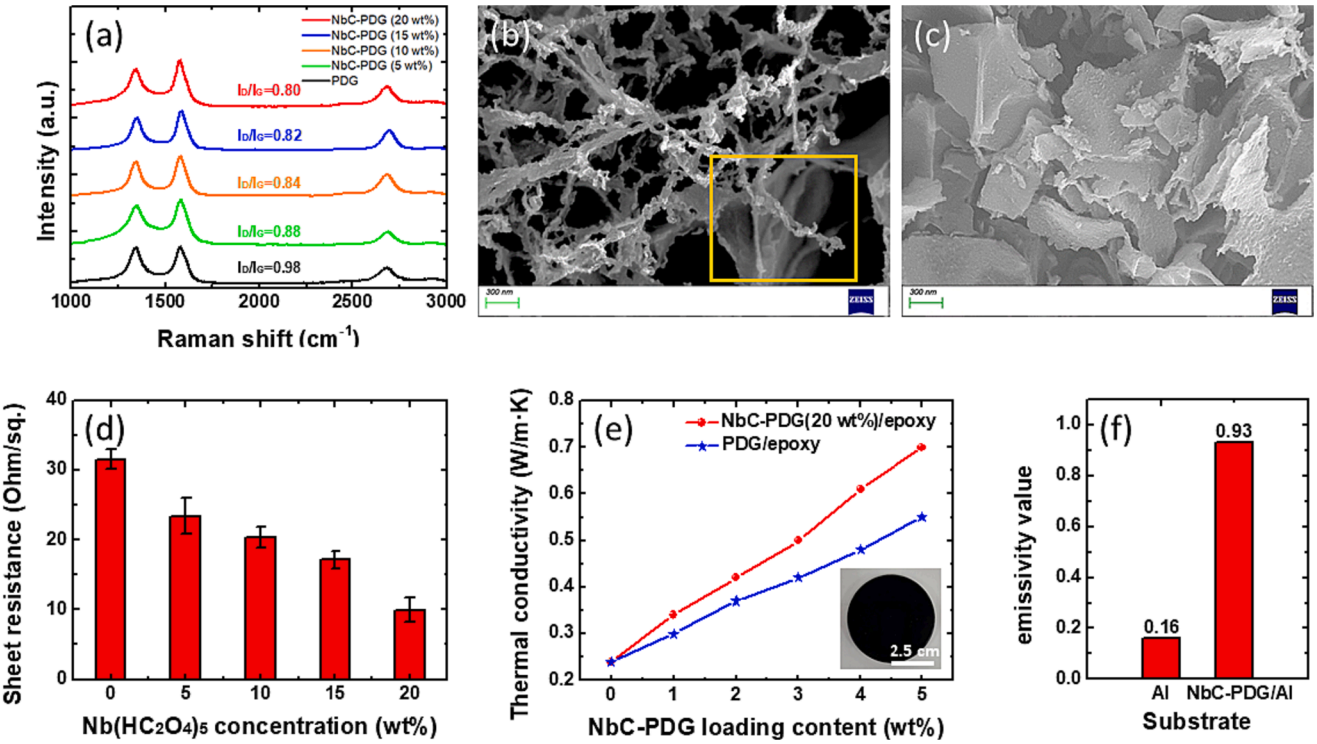

Fig. 4. Transport properties of NbC-PDG. (a) Raman spectra SEM image of (b) PDG. (c) NbC-PDG (20 wt%) (d) sheet resistance of NbC-PDG with various Nb precursor contents (e) thermal conductivity of NbC-PDG/epoxy and PDG/epoxy (inset image of NbC-PDG/epoxy) and (f) surface emissivity of Al and NbC-PDG/Al substrates.

affixed to the bottom center of the modified heat sink using high-purity silver paste to minimize the thermal boundary resistance. Four k-type thermocouples were used to record the temperatures from different regions of the modified heat sink, as shown in Fig. 5b. The temperatures of the electric heater (T_1), bottom (T_2), top center (T_3), and top corner (T_4) of the heat sink were measured in the four regions. Fig. 5c shows the temperature–time profiles of the four regions with an input power of 15 W. The steady-state temperatures (Ts) of T_1, T_2, T_3, and T_4 were 92.6 °C, 80.8 °C, 76.2 °C, and 73.6 °C, respectively. A comparison of the temperature profiles of the bare, PDG-modified and NbC-PDG-modified Al heat sinks in region T_3 is shown in Fig. 5d. The Ts of the bare heat sink was 8.9 and 12.5 °C higher than that of the PDG-modified and NbC-PDG-

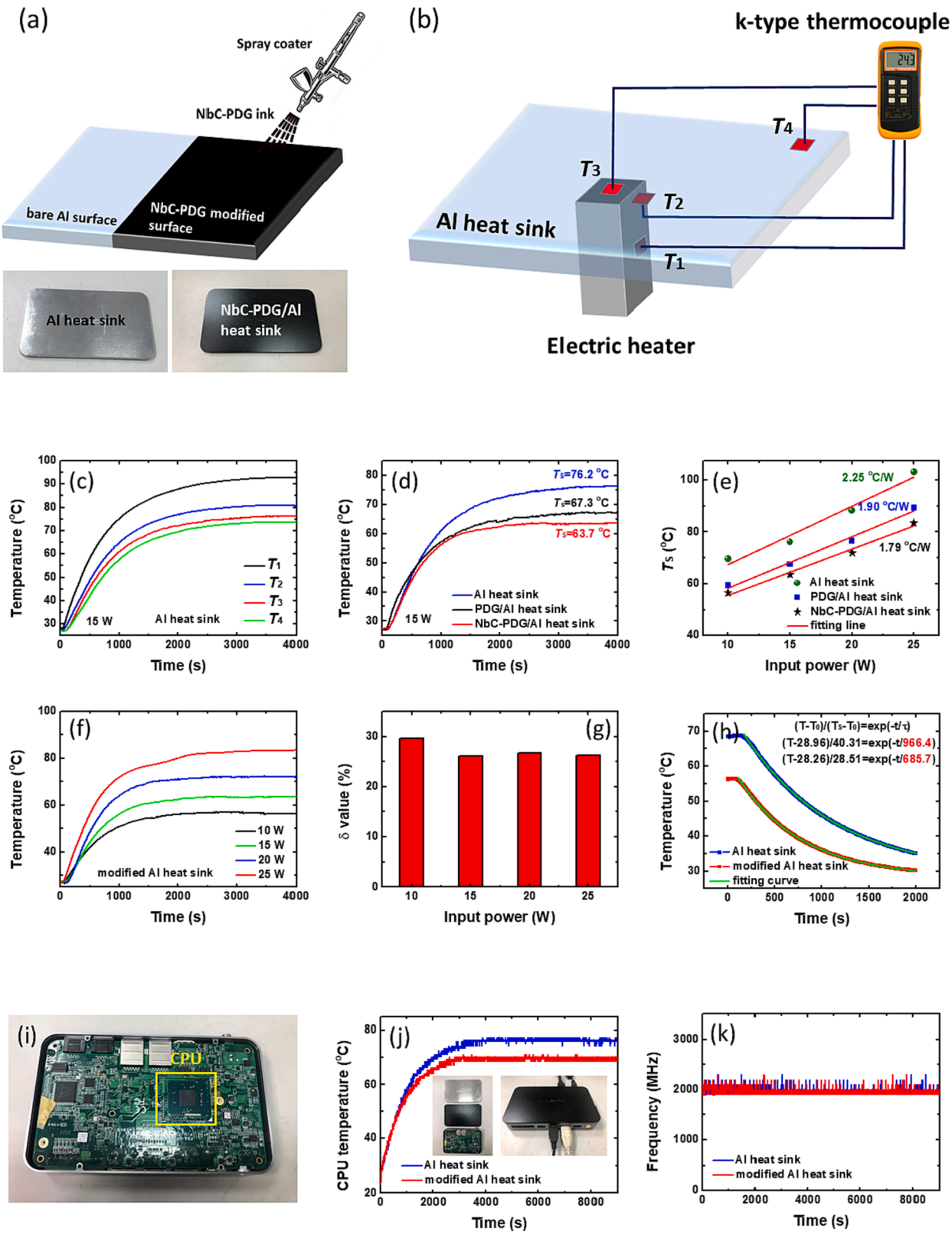

Fig. 5. Heat dissipation performance of NbC-PDG. (a) Modification of Al heat sink with NbC-PDG (inset bare and modified heat sinks) (b) schematic diagram of experimental setup for thermal dissipation evaluation (c) temperature–time profile of bare Al heat sink at different positions (d) temperature profile for bare, PDG-modified and NbC-PDG-modified Al heat sinks at T_3 (e) correlation between *Ts* and input power for the three heat sinks (f) temperature profile and (g) δ value of modified heat sink with various input powers (h) evaluation of cooling rate for two samples (i) photograph of motherboard of IC (j) burn-in test results of IC with different heat sinks (inset images of IC and heat sinks) and (k) frequency of IC during burn-in test.

modified heat sink, respectively. The increases in the temperature as a function of the input power of the three heat sinks was compared, as shown in Fig. 5e. All the heat sinks showed an almost linear behavior, and the bare heat sink exhibits a larger slope than that of the PDG-modified and NbC-PDG-modified sample. In this result, the NbC-PDG coating exhibited better heat dissipation capability.

therefore, in subsequent research, we solely focused on this sample. The temperature profiles of the NbC-PDG-modified heat sink at different input powers are presented in Fig. 5f (the corresponding profiles of the bare Al heat sink and PDG-modified sample are shown in Fig. S3). The cooling efficiency (δ) of the NbC-PDG coating at various input powers was calculated as follows [42]:

$$\delta = \frac{\Delta T}{\Delta T_C} \tag{1}$$

where ΔT and ΔT_C are the difference in the steady-state temperatures of the bare and modified heat sinks and the increase in temperature from the initial temperature of the heat sink, respectively. As shown in Fig. 5g, the average δ value of the NbC-PDG modified heat sink was 27.1 %, i.e., between 26.1 % and 29.6 %. After the heat sink reaches its *T*s, the cooling rate (the heat sinks were allowed to cool down by turning off the power.) was evaluated based on Newton's law of cooling, which is expressed as follows [43]:

$$\frac{T - T_0}{T_S - T_0} = \exp\left(-\frac{t}{\tau}\right) \tag{2}$$

Here, T_0 and τ are the initial temperature and characteristic decay time constant, respectively. The τ values were calculated by fitting the temperature–time profile during the cooling process, as shown in Fig. 5h. The fitted τ values for the bare and modified heat sinks were 966.4 and 685.7 s, respectively. These results clearly indicate that the NbC-PDG coating can enhance thermal radiation and accelerate the

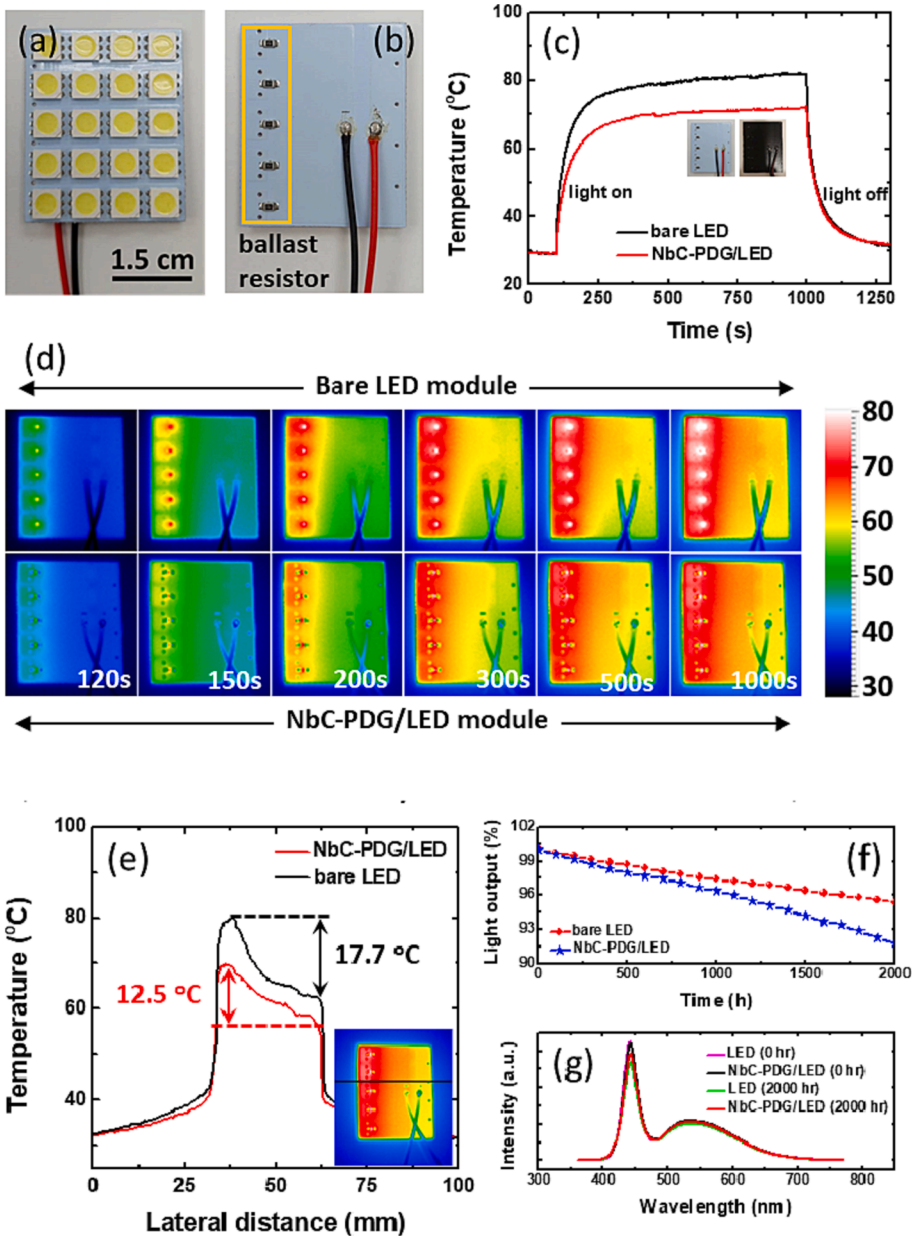

Fig. 6. Effect of NbC-PDG heat sink on LED module. Images of (a) front side and (b) rear side of LED module (c) plot of temperature with respect to time for bare LED and NbC-PDG/LED modules (inset images of bare and NbC-PDG modified LED modules) (d) thermal-imaging photography of bare LED and NbC-PDG/LED modules (e) lateral temperature distribution of two LED modules (f) durability tests of LED modules and (g) emission spectra of LED module recorded before and after durability test.

cooling rate owing to its high emissivity. The adhesion between the NbC-PDG layer and Al substrate was assessed by a cross-cut test. As depicted in Fig. S, the results revealed that only minor flakes of the coating detach at intersections (Class 4B), demonstrating the remarkable adhesive strength. Finally, we tested the practical performance of the NbC-PDG-modified heat sink by incorporating it into an IC. An image of the IC motherboard used in this study is shown in Fig. 5i. The burn-in test results for the IC with different heat sinks are shown in Fig. 5j. In this designed system, the bare and NbC-PDG-modified samples served as a cover and heat sink for the IC, as shown in the inset of Fig. 5j. The *T*s of the IC integrated with the NbC-PDG heat sink decreased by 8.1 °C when the two systems were operated at the same frequency (Fig. 5k). Owing to the development of high-speed computing systems, thermal management has become increasingly important for avoiding overheating and thermal shutdowns. The NbC-PDG-modified heat sink can efficiently remove excess heat from the IC, thus affording energy-saving and rapid computing performance [44].

LEDs are widely used in displays and lighting applications. However, the luminous efficiency of high-power LEDs is only 15 % to 25 % [45]. The remaining 75 %−85 % of the energy is converted into heat energy, thus resulting in an increase in the junction temperature, which adversely affects both their lifespan and efficiency. Hence, the utilization of heat-dissipating materials in high-power LEDs to efficiently transfer excess heat from the LEDs to the surrounding environment is crucial. In this context, we applied the NbC-PDG composite to the rear side of a commercial LED module to validate its effectiveness in dissipating heat. Fig. 6a shows a photograph of the front side of the LED module, which is composed of 20 high-power LED packages with five ballast resistors integrated on the rear side (Fig. 6b). Fig. 6c illustrates the variation in temperature over time at the ballast resistor position for both the bare LED and NbC-PDG/LED modules. After turning on the LED, the temperature of the two modules increased rapidly, and the *T*s values of the bare and NbC-PDG/LED modules after 900 s were 81.9 °C and 72 °C, respectively. Fig. 6d shows consecutive infrared images of the back side of the LED module captured at different time intervals after it was switched on. The highest temperature was observed in the ballast resistor area, thus indicating thermal accumulation on the resistors. These hotspots resulted in a lateral temperature gradient on the entire back side of the LED module. Clearly, modifying the LED module's backside with the NbC-PDG composite can effectively alleviate the degree of thermal accumulation. Compared with the bare LED module, the NbC-PDG/LED module exhibited a much smaller hotspot area at a lower temperature. The lateral temperature distributions of the two modules along the black line (see inset of Fig. 6e) are shown in Fig. 6e. The incorporation of the modified NbC-PDG further reduced the lateral temperature gradient. These results clearly show that the NbC-PDG coating with high emissivity can improve heat dissipation via radiative heat transfer. More importantly, a lower operational temperature can prolong the lifespan of LED modules. As shown in Fig. 6f, the light output of the bare LED module decreased to 91.9 % after 2000 h of testing, whereas the NbC-PDG/LED module maintained a light output of 95.4 %, which indicates a stark contrast. The emission spectra of the two modules after the testing are shown in Fig. 6g. The decrease in the emission intensity of the LED module, as compared with the initial emission spectrum, is attributed to the thermally induced yellowing of the polymeric encapsulant [46].

Energy demand continues to increase worldwide in parallel with economic expansion. LIBs are regarded as the foremost option for clean power storage owing to their high energy and power densities. However, significant heat is generated via electrochemical reactions during the charging and discharging of high-capacity LIBs. Failure to effectively dissipate the generated heat results in to an increase in temperature. When the temperature of LIBs surpasses the designated safety temperature range (60 °C) [47,48], side reactions can be triggered, thus resulting in undesirable consequences such as thermal runaway, electrolyte fires, or explosions. In this study, we applied the NbC-PDG composite to LIBs to enhance their thermal dissipation through radiative heat transfer, which resulted in lower operating temperatures. Specifically, we deposited an NbC-PDG composite on a commercial cylindrical LIB [$LiNi_{0.8}Mn_{0.1}Co_{0.1}O_2$ (NMC811)//graphite] and investigated the effect of the NbC-PDG layer on the operating temperature of the LIB during discharge. Subsequently, we monitored the temperatures in the upper, middle, and lower sections of the cylindrical LIBs (see Fig. 7a). After the LIBs were fully charged, the temperatures of the three regions were recorded during the discharge process at a current of 5C (20 A). The results show that the temperature of the NbC-PDG-coated LIB increased from 26.9 °C to approximately 55.0 °C and that the T4, T5 and T6 values were similar, thus indicating its uniform temperature distribution (Fig. 7b). A comparison of the temperature increase over time for the bare and NbC-PDG-coated LIBs with the corresponding current profiles is presented in Fig. 7c. Photographs of the two samples are shown in the inset of Fig. 7c. The bare LIB reached a maximum temperature of approximately 61.6 °C after a complete discharge at 5C, whereas a lower value of 54.3 °C was indicated for the LIB coated with the NbC-PDG composite. The maximum temperature difference (ΔT_{max}) between the two LIBs after a full discharge under various currents (1–5C) is presented in Fig. 7d. As shown, the dependence of ΔT_{max} between the two samples on the discharge rate indicated a linear relationship, and the ΔT_{max} value increased from 1.4 °C (1C) to 7.5 °C (5C) owing to the improved radiative heat dissipation. The temperature profiles of the NbC-PDG-modified LIB are shown in Fig. 7e. The charge/discharge profiles of the cylindrical LIB at various C-rates are shown in Fig. S5. The results show that the NbC-PDG-coated LIB with a lower operating temperature indicated a higher cycling lifetime than the bare LIB (see Fig. 7f). The capacity retentions of the bare and NbC-PDG-coated LIBs after 500 cycles at 5C were 71.0 % and 80.1 %, respectively.

Recently, $Li_4Ti_5O_{12}$ (LTO) has emerged as a competitive anode material for high-rate and safe LIBs owing to its spinel structure, which provides 3D transportation pathways for Li^+ ions and a high operating voltage of 1.55 V (vs. Li/Li^+). However, severe gassing during charge/discharge cycles and storage, particularly at elevated temperatures, hinders the widespread development of LTO-based LIBs [49]. In this study, we improved the thermal dissipation characteristics of soft-packed LTO-based LIBs by depositing an NbC-PDG layer. Specifically, we fabricated soft-packed LTO-based LIBs using commercial $LiNi_{0.6}Mn_{0.2}Co_{0.2}O_2$ (NMC622) and a high-rate LTO developed by our group [50] as the cathode and anode materials, respectively. The charge/discharge profiles of the NMC622//LTO LIB with a designed capacity of 1000 mAh and tested at different C rates are shown in Fig. 8a. The soft-packed NMC622//LTO LIB delivered a capacity of 947 mAh at 0.1C, which is almost identical to its designed value. Even under charge/discharge at a high rate of 10C, the LIB afforded a capacity of 728.2 mAh, thus indicating its excellent rate capability. To monitor the surface temperature of the soft-packed LIBs, the NMC//LTO LIBs were continuously cycled between 2.7 and 1.5 V at a current density of 10C for 100 cycles. During the repetitive cycling, the surface temperature of the soft-packed LIBs was recorded using an infrared thermograph, and the results are presented in Fig. 8b). As shown, the surface-modified LIB shows a lower temperature (49.2 °C) than the bare LIB (58.1 °C) after the repetitive cycling. The maximum temperatures (T_{max}) of the two soft-packed LIBs recorded at various C rates after 100 cycles are shown in Fig. 8c. The T_{max} value of the bare LIB exceeded that of the NbC-PDG-modified LIB, thus suggesting improved heat dissipation by radiation. Thermal infrared images of the bare and modified LIBs at 10C are shown in Fig. 8d and 8e, respectively. The images show that the deposited NbC-PDG layer not only efficiently reduced the temperature, but also uniformly distributed the temperature on the LIB surface. The lower temperature with a more even distribution of the modified NMC622//LTO LIB can suppress gassing during the charge/discharge process. As shown in Fig. 8f, the expansion rate of the bare NMC622//LTO was 86.1 % after 200 cycles, which was 1.37 times higher that of the NbC-PDG-modified LIB (63 %) owing to its higher operation temperature. Digital

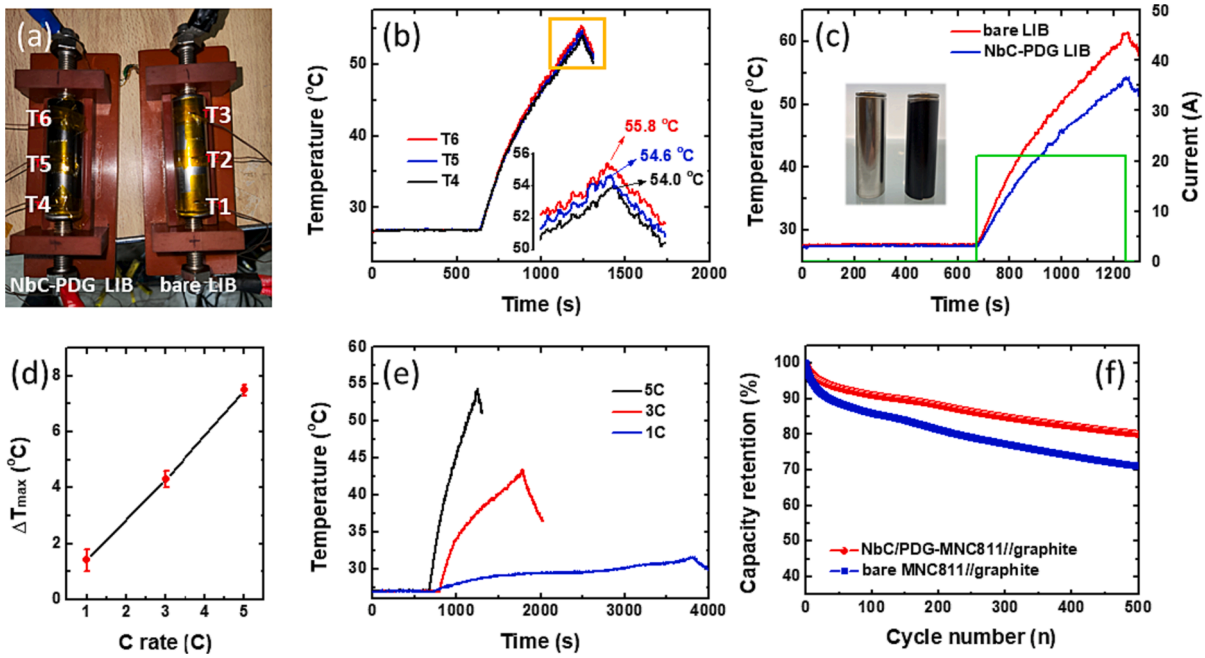

Fig. 7. Effect of NbC-PDG heat sink on NMC811//graphite cylindrical LIB. (a) Experimental setup and equipment used to evaluate temperature of cylindrical LIBs at different positions (b) temperature profile of NbC-PDG LIB at different positions (c) comparison of temperature profiles of bare and NbC-PDG-modified LIBs (inset images of bare and modified LIBs) (d) plot of ΔT_{max} with respect to C rate for two LIBs (e) corresponding temperature profiles of NbC-PDG-modified LIB with various C rates and (f) cycling stability of two LIBs.

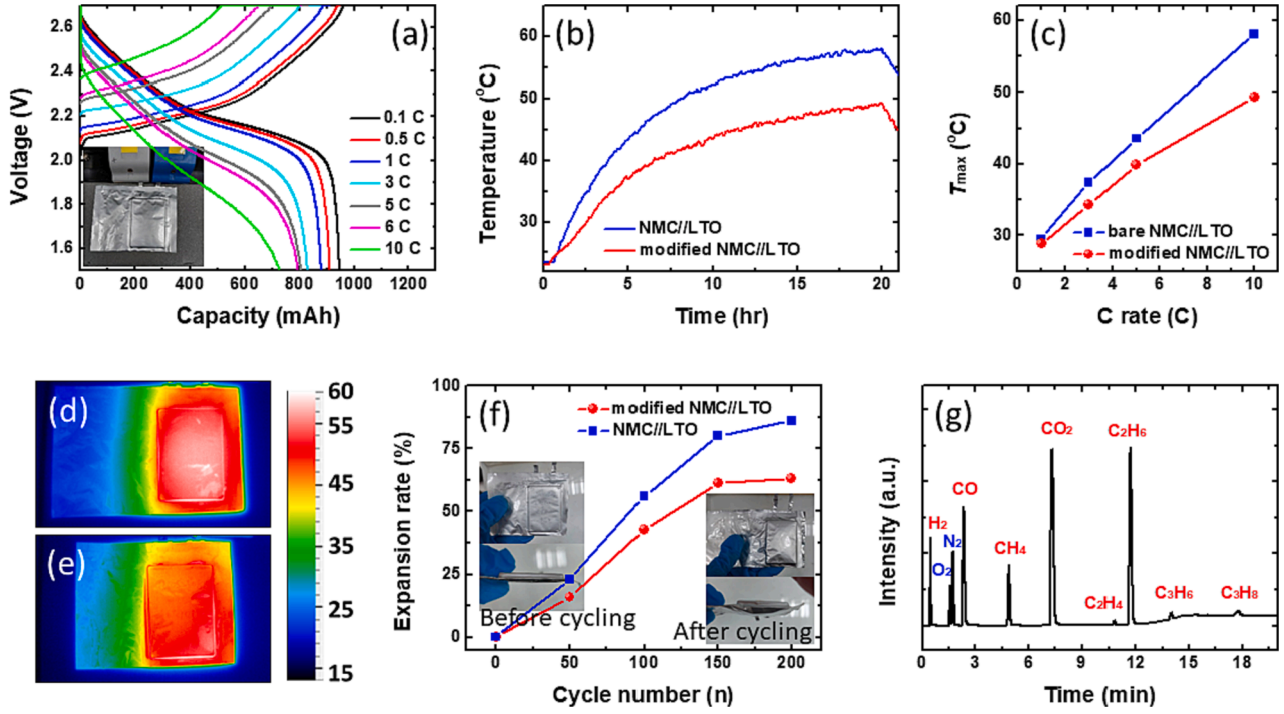

Fig. 8. Effect of NbC-PDG heat sink on NMC622//LTO soft-packed LIB. (a) Charge/discharge profiles of NMC622//LTO LIB with various C rates (inset image of soft-packed LIB during charge/discharge process) (b) surface temperature of LIB during continuous charge/discharge process between 2.7 and 1.5 V at current density of 10C for 100 cycles (c) plot of T_{max} with respect to C rate for two soft-packed LIBs thermal infrared images of (d) bare and (e) NbC-PDG-modified LIBs (f) expansion rate of two LIBs (inset images of LIB before and after cycling) and (g) GC-BID chromatogram of gases formed during repetitive cycling.

photographs of the NMC622//LTO LIB before and after cycling are shown in the inset of Fig. 8f. The chemical components of the gas species generated from the NMC622//LTO LIB were analyzed via gas chromatography-barrier discharge ionization detection (GC-BID), as shown in Fig. 8g. H_2, CO, CO_2 and some hydrocarbons such as CH_4, C_2H_4, C_2H_6, C_3H_6 and C_3H_8 were the major components, which is consistent with previous results [51,52].

Owing to its broadband absorption capability [53–55], the NbC-PDG can be used as a light-to-heat conversion nanomaterial for water purification and desalination. In this study, we deposited an NbC-PDG

composite on a commercial macroporous MS (NbC-PDG/MS) via spray coating, which can be utilized as an efficient solar–thermal conversion medium. In the designed construction, the 3D porous skeleton of the MS increased the surface area for solar absorption, with multiple scatterings and decreased reflections [56]. The UV–vis-NIR absorption spectrum of NbC-PDG is shown in Fig. S6. The solar-driven water evaporation and desalination properties of the modified sponge were demonstrated. The experimental setup is shown in Fig. 9a. The bare and modified MS were placed in a glass container with an opening on top, and a transparent glass lid was positioned atop the desalination apparatus. Under solar irradiation, the water thermally vaporized by the NbC-PDG/MS can be naturally condensed on the transparent glass cover and accumulated at the bottom. Digital photographs of MS with different coating numbers and the corresponding water contact angles are shown in Fig. 9b. The MS surface exhibited hydrophobic properties after NbC-PDG modification. The contact angle of the MS increased from 111.5° to 123.5° as the number of coatings increased. However, the water droplet was immediately absorbed by the pure MS sponge and the contact angle cannot be measured. Additionally, the surface morphology of the NbC-PDG/MS was investigated via SEM, as shown in Fig. 9c. Open macropores with 3D structures were maintained after the NbC-PDG modification. Furthermore, the NbC-PDG/MS showed a much rougher surface with many nanoparticles decorated on the MS compared with the bare MS (Fig. S7). The SEM images with higher magnification are also provided in Fig. S8. Fig. 9d shows the water evaporation rate of the modified MS with different coating numbers under 1 sun illumination. The changes in water evaporation mass for the various modified MS samples are illustrated in Fig. 9e. The modified MS coated with NbC-PDG exhibited the highest evaporation rate of 1.23 kg/m^2 h. Moreover, a comparison of the correlation between the solar evaporation rate and solar intensity of the bare and modified MS is presented in Fig. 9f. The evaporation rates of both samples increased linearly with the solar intensity. The slope of the NbC-PDG/MS extracted from Fig. 9f was 5.46 times larger than that of the bare sample, thus indicating its improved solar–vapor conversion efficiency. Finally, the seawater desalination and water purification capabilities of the modified MS were evaluated. Fig. 9g shows the

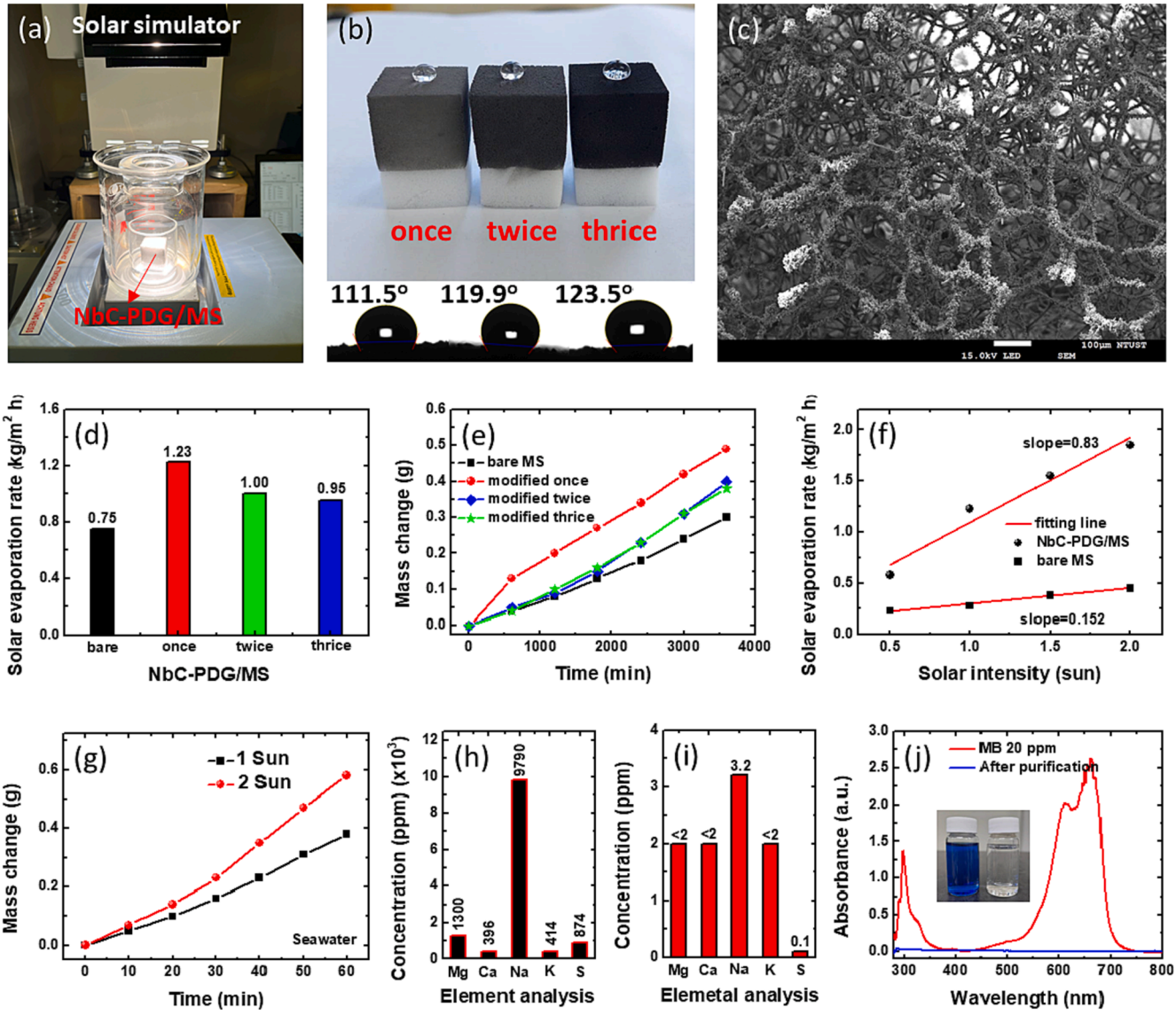

Fig. 9. Solar–thermal conversion performance of NbC-PDG/MS. (a) Experimental setup used to evaluate solar–thermal conversion capability of NbC-PDG/MS (b) images of NbC-PDG/MS showing their coating numbers and corresponding water contact angles (c) SEM image of modified MS (d) solar evaporation rate and (e) corresponding mass change of NbC-PDG/MS with different coating numbers (f) plot of solar evaporation rate with respect to solar intensity (g) seawater mass change of NbC-PDG/MS with different solar intensities ICP analysis of seawater (h) before and (i) after desalination (j) absorbance spectrum of MB solution before and after solar-driven purification (inset the MB solution before and after purification).

seawater mass changes exhibited by the NbC-PDG/MS at 1 and 2 sun. Based on the mass change – time profile, the seawater evaporation rates of the NbC-PDG/MS were 0.95 and 1.45 kg/m^2·h at 1 and 2 suns, respectively. To assess the quality of the desalinated water, the concentrations of five major elements (Mg, Ca, Na, K, and S) were measured via ICP analysis both before and after desalination. As shown in Fig. 9h and 9i, the concentrations of the five elements in the desalinated water reduced to relatively low levels. The salinity level established by the World Health Organization is 103 ppm, which is significantly higher than that of our desalinated water samples [57]. The solar-driven water purification capability of the modified MS was examined in the same manner. The quality of the purified water obtained from methylene blue (MB) solution was confirmed by measuring the optical absorption spectrum, as shown in Fig. 9j. The clean water exhibited near-zero optical absorbance between 300 and 800 nm, thus indicating the successful removal of MB.

4. Conclusion

In this study, we successfully prepared a PDG decorated with NbC nanoparticles via CO_2 laser scribing approach. The as-prepared NbC-PDG composite possessed a greater degree of graphitization and higher conductivity than bare PDG. When combining the NbC-PDG with epoxy to form a composite, the resulting NbC-PDG/epoxy demonstrated better thermal conductivity (0.70 W/m·K) than PDG/epoxy (0.55 W/m·K). By depositing the NbC-PDG composite onto the conventional Al heat sink, the *T*s value reduced by 12.5 °C as compared with the case of a bare Al heat sink consequently, an average δ value of 27.1 % was achieved via radiative heat dissipation. Utilizing the NbC-PDG as a heat sink can result in reduced operating temperatures and a more homogeneous temperature distribution in ICs, LED modules, and LIBs, thereby enhancing their performance, lifespan, and cycling stability. In addition, we fabricated an NbC-PDG-modified MS for efficient solar-driven desalination and water purification. Benefitting from the broadband absorption and excellent photothermal properties of the NbC-PDG composite, the water evaporation rate of the NbC-PDG/MS was 5.46 times larger than that of bare MS. Additionally, the modified MS also demonstrated remarkable desalination and water purification capabilities.

CRediT authorship contribution statement

Yu-Sheng Hsiao: Conceptualization, Formal analysis, Funding acquisition, Investigation, Project administration, Resources, Supervision, Writing – original draft, Writing – review & editing. **Chao-Yuan Lin:** Data curation, Formal analysis. **Lin-Yang Weng:** Data curation, Formal analysis, Investigation. **Chun-Han Hsu:** Data curation, Formal analysis, Investigation, Methodology. **Ta-Hung Cheng:** Data curation, Formal analysis, Investigation. **Jen-Hsien Huang:** Conceptualization, Data curation, Formal analysis, Investigation, Methodology, Resources. **Nian-Jheng Wu:** Data curation, Formal analysis. **Wei Kong Pang:** Supervision. **Shih-Chieh Hsu:** Supervision. **Huei Chu Weng:** Supervision. **Yu-Ching Huang:** Conceptualization, Formal analysis, Funding acquisition, Investigation, Project administration, Resources, Supervision, Writing – original draft, Writing – review & editing.

Declaration of competing interest

The authors declare that they have no known competing financial interests or personal relationships that could have appeared to influence the work reported in this paper.

Data availability

The data that has been used is confidential.

Acknowledgments

These research endeavors were supported by the National Science and Technology Council (NSTC) of Taiwan (grant nos. MOST 111-2628-E-011-003-MY2).

Appendix A. Supplementary data

Supplementary data to this article can be found online at https://doi.org/10.1016/j.cej.2024.149007.

References

[1] Z. He, Y. Yan, Z. Zhang, Thermal management and temperature uniformity enhancement of electronic devices by micro heat sinks: a review, Energy 216 (2021) 119223.
[2] Z. Zhang, X. Wang, Y. Yan, A review of the state-of-the-art in electronic cooling, e-Prime 1 (2021) 100009.
[3] J. Mathew, S. Krishnan, A review on transient thermal management of electronic devices, J. Electron. Packag. 144 (2022) 010801.
[4] R.J. Warzoha, A.A. Wilson, B.F. Donovan, N. Donmezer, A. Giri, P.E. Hopkins, S. Choi, D. Pahinkar, J. Shi, S. Graham, Z. Tian, L. Ruppalt, Applications and impacts of nanoscale thermal transport in electronics packaging, J. Electron. Packag. 143 (2021) 020804.
[5] H.J. Xu, Z.B. Xing, F.Q. Wang, Z.M. Cheng, Review on heat conduction, heat convection, thermal radiation and phase change heat transfer of nanofluids in porous media: fundamentals and applications, Chem. Eng. Sci. 195 (2019) 462–483.
[6] G. Zhang, S. Jiang, H. Zhang, W. Yao, C. Liu, Excellent heat dissipation properties of the super-aligned carbon nanotube films, RSC Adv. 6 (2016) 61686–61694.
[7] A.M. Hadi, M.A. Ismael, H.A. Alhattab, Experimental investigation of thermal performance of the graphene-coated Al heat sink, Mater. Today Proc. 42 (2021) 2779–2784.
[8] S. Şevik, B. Çiçek, Ö. Özdilli, T. Aydoğmuş, Z. Özer, Thermal performance analysis of aluminum, copper, and graphene nanoplatelets-doped nanocomposite heat sinks manufactured via stereolithography, Appl. Therm. Eng. 226 (2023) 120315.
[9] C.B. Kim, J. Lee, J. Cho, M. Goh, Thermal conductivity enhancement of reduced graphene oxide via chemical defect healing for efficient heat dissipation, Carbon 139 (2018) 386–392.
[10] R. Navik, H. Tan, H. Zhang, Z. Liu, Q. Xiang, L. Shi, S. Lu, Y. Zhao, Scalable production of polyamide-6/graphene composites with enhanced electromagnetic shielding and thermal conductivity, Chem. Eng. J. 471 (2023) 144445.
[11] Y. Zou, Y. Wang, H. Zhang, D. Wei, T. Jin, H. Wang, S. Liao, D. Jia, Y. Zhou, Al_2O_3/reduced graphene oxide double-layer radiative coating for efficient heat dissipation, Mater. Des. 157 (2018) 130–140.
[12] Z. Gao, Y. Zhang, Y. Fu, M.M.F. Yuen, J. Liu, Thermal chemical vapor deposition grown graphene heat spreader for thermal management of hot spots, Carbon 61 (2013) 342–348.
[13] J.S. Lee, T. Kim, H.H. Lee, Y.H. Kim, Efficient heat dissipation by ion-mediation assembled reduced graphene oxide, J. Mater. Chem. C 6 (2018) 2515–2521.
[14] G. Choi, M. Yun, W.T. Hsu, D.I. Shim, D. Lee, B.S. Kim, H.H. Cho, Enhanced boiling heat transfer by nucleation patterning with self-assembly of reduced graphene oxide coating, Int. J. Heat Mass Transf. 197 (2022) 123329.
[15] N. Han, T.V. Cuong, M. Han, B.D. Ryu, S. Chandramohan, J.B. Park, J.H. Kang, Y. J. Park, K.B. Ko, H.Y. Kim, H.K. Kim, J.H. Ryu, Y.S. Katharria, C.J. Choi, C.H. Hong, Improved heat dissipation in gallium nitride light-emitting diodes with embedded graphene oxide pattern, Nat. Commun. 4 (2013) 1452.
[16] J. Lin, Z. Peng, Y. Liu, F. Ruiz-Zepeda, R. Ye, E.L.G. Samuel, M.J. Yacaman, B. I. Yakobson, J.M. Tour, Laser-induced porous graphene films from commercial polymers, Nat. Commun. 5 (2014) 5714.
[17] S. Aslam, R.U.R. Sagar, Y. Liu, T. Anwar, L. Zhang, M. Zhang, N. Mahmood, Y. Qiu, Graphene decorated polymeric flexible materials for lightweight high areal energy lithium-ion batteries, Appl. Mater. Today 17 (2019) 123–129.
[18] M. Khandelwal, C.V. Tran, J. Lee, J.B. In, Nitrogen and boron co-doped densified laser-induced graphene for supercapacitor applications, Chem. Eng. J. 428 (2022) 131119.
[19] M. Abdulhafez, G.N. Tomaraei, M. Bedewy, Fluence-dependent morphological transitions in laser-induced graphene electrodes on polyimide substrates for flexible devices, ACS Appl. Nano Mater. 4 (2021) 2973–2986.
[20] B. Zhu, L. Yu, S. Beikzadeh, S. Zhang, P. Zhang, L. Wang, J. Travas-Sejdic, Disposable and portable gold nanoparticles modified - laser-scribed graphene sensing strips for electrochemical, non-enzymatic detection of glucose, Electrochim. Acta 378 (2021) 138132.
[21] M.R. Bobinger, F.J. Romero, A. Salinas-Castillo, M. Becherer, P. Lugli, D. P. Morales, N. Rodríguez, A. Rivadeneyra, Flexible and robust laser-induced graphene heaters photothermally scribed on bare polyimide substrates, Carbon 144 (2019) 116–126.
[22] Y. Ouyang, L. Bai, H. Tian, X. Li, F. Yuan, Recent progress of thermal conductive ploymer composites Al_2O_3 fillers, properties and applications, Compos. Part A Appl. Sci. 152 (2022) 106685.
[23] Z. Han, A. Fina, Thermal conductivity of carbon nanotubes and their polymer nanocomposites: a review, Prog. Polym. Sci. 36 (2011) 914–944.

[24] C.T. Yang, H.I. Hsiang, T.S. Huang, P.C. Huang, Y.K. Han, Thermal conductivity and dielectric properties of PEDOT:PSS-AlN filler reinforced water-soluble polymer composites, Ceram. Int. 43 (2017) S710–S716.
[25] W. Kong, Z. Wang, N. Casey, M.M. Korah, A. Uppal, M.D. Green, K. Rykaczewski, R.Y. Wang, High thermal conductivity in multiphase liquid metal and silicon carbide soft composites, Adv. Mater. Interfaces 8 (2021) 2100069.
[26] R. Kang, Z. Zhang, L. Guo, J. Cui, Y. Chen, X. Hou, B. Wang, C.T. Lin, N. Jiang, J. Yu, Enhanced thermal conductivity of epoxy composites filled with 2D transition metal carbides (MXenes) with ultralow loading, Sci. Rep. 9 (2019) 9135.
[27] T. Amriou, B. Bouhafs, H. Aourag, B. Khelifa, S. Bresson, C. Mathieu, FP-LAPW investigations of electronic structure and bonding mechanism of NbC and NbN compounds, Phys. B Condens. Matter 325 (2003) 46–56.
[28] Y. Zhong, X. Xia, F. Shi, J. Zhan, J. Tu, H.J. Fan, Transition metal carbides and nitrides in energy storage and conversion, Adv. Sci. 3 (2016) 1500286.
[29] A. Kundu, J. Ma, J. Carrete, G.K.H. Madsen, W. Li, Anomalously large lattice thermal conductivity in metallic tungsten carbide and its origin in the electronic structure, Mater. Today Phys. 13 (2020) 100214.
[30] J. Ma, M. Wu, Y. Du, S. Chen, W. Jin, L. Fu, Q. Yang, A. Wen, Formation of nanocrystalline niobium carbide (NbC) with a convenient route at low temperature, J. Alloys Compd. 475 (2009) 415–417.
[31] D. Ji, X. Xu, L. Jiang, S. Amirjalayer, L. Jiang, Y. Zhen, Y. Zou, Y. Yao, H. Dong, J. Yu, H. Fuchs, W. Hu, Surface polarity and self-structured nanogrooves collaborative oriented molecular packing for high crystallinity towards efficient charge transport, J. Am. Chem. Soc. 139 (2017) 2734–2740.
[32] C. Zhang, X. Zhu, Z. Wang, P. Sun, Y. Ren, J. Zhu, J. Zhu, D. Xiao, Facile synthesis and strongly microstructure-dependent electrochemical properties of graphene/manganese dioxide composites for supercapacitors, Nanoscale Res. Lett. 9 (2014) 490.
[33] L.X. Yang, H.L. Zhang, Y. Wang, H.J. Liu, C.L. Zeng, A novel and simple method for large-scale synthesis of nanosized NbC powder by disproportionation reaction in molten salt, Ceram. Int. 45 (2019) 3791–3796.
[34] T.G. Woo, I.S. Park, K.H. Jung, W.Y. Jeon, K.W. Seol, Effect of N_2 plasma treatment on the adhesion of Cu/Ni thin film to polyimide, Met. Mater. Int. 17 (2011) 789–795.
[35] A. Pajares, P. R. Piscina, N. Homs, Catalytic behaviour of transition metal carbides of group 5 in the methanol steam reforming, Int. J. Hydrog. Energy, https://doi.org/10.1016/j.ijhydene.2023.06.017.
[36] J. Hao, J. Xu, S. Peng, S. Jiang, Z. Xie, P.R. Munroe, Dissecting anticorrosion and antimicrobial potency of an ag nanoparticle/nbc nanocomposite coating in a marine environment containing sulfate-reducing bacteria, ACS EST Engg. 2 (2022) 1386–1402.
[37] A. Gupta, M. Mittal, M.K. Singh, S.L. Suib, O.P. Pandey, Low temperature synthesis of NbC/C nano-composites as visible light photoactive catalyst, Sci. Rep. 8 (2018) 13597.
[38] Y. Peng, W. Zhao, F. Ni, W. Yu, X. Liu, Forest-like laser-induced graphene film with ultrahigh solar energy utilization efficiency, ACS Nano 15 (2021) 19490–19502.
[39] L.X. Duy, Z. Peng, Y. Li, J. Zhang, Y. Ji, J.M. Tour, Laser-induced graphene fibers, Carbon 126 (2018) 472–479.
[40] S. Wang, L. Shao, L. Yu, J. Guan, X. Shi, Z. Sun, J. Cai, H. Huang, A. Trukhanov, Niobium Carbide as a Promising Pseudocapacitive Sodium-Ion Storage Anode, 9 (2021) 2100298.
[41] C.N. Suryawanshi, T. Kim, C.T. Lin, An instrument for evaluation of performance of heat dissipative coatings, Rev. Sci. Instrum. 81 (2010) 035105.
[42] Y. Weng, S. Wu, L. Wang, W. Zhao, Y. Jiang, Y. Deng, An efficient cooling solution with 3D interconnected graphene architectures for passive heat dissipation, J. Mater. Chem. C 10 (2022) 13167–13173.
[43] J. Yan, Y.G. Jeong, Multiwalled carbon nanotube/polydimethylsiloxane composite films as high performance flexible electric heating elements, Appl. Phys. Lett. 105 (2014) 051907.
[44] N.A. Pambudi, A. Sarifudin, R.A. Firdaus, D.K. Ulfa, I.M. Gandidi, R. Romadhon, The immersion cooling technology Current and future development in energy saving, Alex. Eng. J. 61 (2022) 9509–9527.
[45] Y.F. Zhang, Y.J. Ren, S.L. Bai, Vertically aligned graphene film/epoxy composites as heat dissipating materials, Int. J. Heat Mass Transf. 118 (2018) 510–517.
[46] M. Cai, Z. Liang, Y. Qin, J. Fan, D. Ma, D. Yang, G. Zhang, Effects of silicone lens aging on degradation kinetics of light-emitting diode package in various accelerated testing, Opt. Mater. 107 (2020) 110071.
[47] N. Mei, X. Xu, R. Li, Heat dissipation analysis on the liquid cooling system coupled with a flat heat pipe of a lithium-ion battery, ACS Omega 5 (2020) 17431–17441.
[48] R.R. Kohlmeyer, G.A. Horrocks, A.J. Blake, Z. Yu, B. Maruyama, H. Huang, M. F. Durstock, Pushing the thermal limits of Li-ion batteries, Nano Energy 64 (2019) 103927.
[49] C. Han, Y.B. He, M. Liu, B. Li, Q.H. Yang, C.P. Wong, F. Kang, A review of gassing behavior in $Li_4Ti_5O_{12}$-based lithium ion batteries, J. Mater. Chem. A 5 (2017) 6368–6381.
[50] C.W. Chang-Jian, B.C. Ho, C.K. Chung, J.A. Chou, C.L. Chung, J.H. Huang, J. H. Huang, Y.S. Hsiao, Doping and surface modification enhance the applicability of $Li_4Ti_5O_{12}$ microspheres as high-rate anode materials for lithium ion batteries, Ceram. Int. 44 (2018) 23063–23072.
[51] C.R. Fell, L. Sun, P.B. Hallac, B. Metz, B. Sisk, investigation of the gas generation in lithium titanate anode based lithium ion batteries, J. Electrochem. Soc. 162 (2015) A1916.
[52] J. Liu, P. Bian, J. Li, W. Ji, H. Hao, A. Yu, Gassing behavior of lithium titanate based lithium ion batteries with different types of electrolytes, J. Power Sources 286 (2015) 380–387.
[53] H. Ren, M. Tang, B. Guan, K. Wang, J. Yang, F. Wang, M. Wang, J. Shan, Z. Chen, D. Wei, H. Peng, Z. Liu, Hierarchical graphene foam for efficient omnidirectional solar–thermal energy conversion, Adv. Mater. 29 (2017) 1702590.
[54] Y. Yang, R. Zhao, T. Zhang, K. Zhao, P. Xiao, Y. Ma, P.M. Ajayan, G. Shi, Y. Chen, Graphene-based standalone solar energy converter for water desalination and purification, ACS Nano 12 (2018) 829–835.
[55] K. Peng, J. Ye, H. Wang, H. Song, B. Deng, S. Song, Y. Wang, L. Zuo, J. Ye, Natural halloysite nanotubes supported Ru as highly active catalyst for photothermal catalytic CO_2 reduction, Appl. Catal. B Environ. 324 (2023) 122262.
[56] C. Chang, M. Liu, L. Li, G. Chen, L. Pei, Z. Wang, Y. Ji, Salt-rejecting rGO-coated melamine foams for high-efficiency solar desalination, J. Mater. Res. 37 (2022) 294–303.
[57] World Health Organization, Guidelines for Drinking-Water Quality. Fourth Edition, World Health Organization, Geneva, Switzerland 2011.